Answer to reviewer 1

1 Introduction

Thank you for the opportunity to peer review the manuscript "High Spatial and temporal 3D Sea Ice Thickness Reconstruction using Seismic Waveform Inversion and Tomography" by Zandi et al. (2016).

This manuscript presents a novel method of capturing and monitoring the small-scale heterogeneities of sea ice thickness using seismic methods. Utilizing that the frequency of flexural waves in sea ice is highly dependent on the ice thickness, an inversion algorithm is used to derive the ice thickness from vibrations measured with geophone arrays. The novelty is two-part. Firstly, the Spectral Element Method (SEM) is used to compute theoretical waveforms for a range of source-receiver distances and ice thicknesses, thereby building up a matchup-database for quicker computations. Secondly, multiple source-receiver paths are combined to form a high resolution ice thickness map using tomography. The method is applied on two different field campaigns, one with active/controlled sources and another with passive sources, e.g., icequakes. The results show thicknesses that are consistent with drillhole measurements, although negatively biased due layering in the ice, and an example of how this method could be used for autonomous monitoring of a selected area.

I do not have a background within seismology, so my review focuses on the field setup and sea ice properties rather than the theoretical wave equations. The review is structured in 4 major parts. The first part is related to validating the results, the second part is on potential biases in the experiment setup, and the third part discusses potential up-scaling. The fourth part is a list of minor comments before the conclusion.

We thank the reviewer for the careful and constructive reading of the manuscript. Please find below our answers to the comments

2 Validation of results

2.1 Ice thicknesses

From line 110, the average ice thickness from the two ice types in the controlled-source setup are provided from drillhole measurements, 50±5 cm and 70±5 cm, respectively. Here I suggest stating how many drillholes the estimates are based on and what the uncertainties indicate. Are they uncertainties in the tape reading or the spread of a thickness distribution? Later on in Figure 8a, there are shown 9 drillhole measurements within the area of interest, but only 6 of them are shown in Figure 8b, and with only one measurement in the thickest ice.

Ice thickness was measured through drill holes at five points per region along a 600 m optical fiber spanning three distinct ice types (0–∼175 m, 175–∼320 m, and 320–600 m; see Fig. 8a and Kuchly et al., 2026, Fig. 1). Figure 8a shows the 13 drill holes located within the area of the tomography, while Figure 8b zooms in on the 240–380 m segment and displays the six drill holes located within that segment. The reported ±5 cm uncertainty reflects natural thickness variability within each region rather than measurement error.

The manuscript has been clarified to explain the limitations of the validation, the independent DAS validation, the constraints on collecting additional measurements, and the meaning of the reported uncertainty. The following text has been added to section *Controlled source data*:

The reported ±5 cm uncertainty reflects natural thickness variability within each region rather than measurement error.

and later in section *Inversion of controlled sources in Canada*

The validation is limited to a single transect crossing three ice regions. Drill holes were made along this transect, and the thickness values measured in the area of the tomography are shown

in Figure Figure 8: 13 drill holes in panel a and 6 in panel b, which zooms in on the 240–380 m segment. The transect was independently validated by DAS inversion in Kuchly et al. (2026). More thickness measurements away from this transect would of course strengthen the validation of the 2D map, but they could not be collected within the time available during the field campaign, in which the same set of geophones was installed and removed several times within a day for the linear and 2D arrays, in parallel with other experiments.

Kuchly et al. (2026), another submitted manuscript on the same field campaign, describes the thick ice as "a rough jumble of ice fragments with irregularities about 20 cm high" and with an average thickness of 72 cm. Their thin ice has an average thickness of 54 cm. Furthermore, their colorbar in Figure 1b is cropped at 0.9 m, showing more variability in the thick ice thickness than in Figure 8b mentioned before. I am wondering why there are such discrepancies between the two descriptions given the significant overlap of co-authors.

We thank the reviewer for bringing this to our attention. The reviewer refers to the preprint version of Kuchly et al. (2026), which did not provide uncertainties. The revised (and accepted) version now provides average values and associated uncertainties, linked to the natural thickness variability: 72 ±10 cm for thick ice and 54 ±4 cm for thin ice. Hence we want to clarify that there is no discrepancy in the underlying measurement data between the two manuscripts. Both studies rely on the exact same set of physical drill-hole measurements. The average values, and associated uncertainties reported in Kuchly et al. (2026) fall directly within the thickness ranges provided in our text.

The apparent visual differences are simply a result of spatial zooming and tailored colormap choices suited to each paper's specific analytical focus. While Kuchly et al. (2026) (Fig. 1b) show the entire 600 m profile using a broad red-to-blue colormap scaled up to 0.9 m (where some of drill-hole measurements, e.g., that on the far left of region R2, fall outside our 35–70 cm range), our Figure 8b focuses strictly on the selected 240–380 m tomography inversion area. Within this specific zone, all drill-hole measurements and tomography results fall between 35 cm and 70 cm. We selected a sequential "Blues" colormap bounded to this 35–70 cm range to specifically better highlight the dominant spatial variations resolved by the tomography.

However, we agree that the average values and uncertainties reported in our manuscript (70 ±5 cm for thick ice and 50 ±5 cm) do not match exactly those given in Kuchly et al. (2026) (72 ±10 cm for thick ice and 54 ±4 cm). For clarity, we have therefore modified the values in our manuscript to match those in Kuchly et al. (2026), even though the compared areas are not exactly the same.

2.2 Source positions

I like the stepwise fine-tuning of inverted positions in the 5 step inversion method which shows clear improvements in Figure 9. For the controlled-source setup, it is stated on line 308 that these steps are skipped due to the source positions being known. In the data description, I suggest a description of how these positions were measured in the field.

The reviewer is right. The true source positions were measured with GPS readings. We have added the following text to the data description:

These source positions were measured with GPS readings.

Also, I see this as a great opportunity to validate step 2 and 3 in Algorithm 1, and I suggest doing a comparison between estimated and actual source positions to assess the uncertainties of the triangulation (or "quintangulation").

We thank the reviewer for this valuable suggestion. The inversion of artificial source positions was investigated in detail in Moreau et al. (2020b) (open access), assuming a constant ice thickness for all source–receiver paths, which corresponds to step 2 of our algorithm. That study reported absolute source-location errors of approximately 5 m. Since the present algorithm further reduces the waveform misfit by approximately 20–30%, we did not anticipate a significant degradation of the source-location accuracy. Nevertheless, we agree that an independent

validation is worthwhile.

Although we prefer not to include this additional analysis in the manuscript, which is already quite dense, we performed the suggested comparison between the actual and inverted source positions. Figure 1 shows the actual source positions (black circles) and the inverted positions (red crosses) obtained with our algorithm for each processed source. For the inversions, we selected the four corner stations together with one station located near the centre of the array. The mean absolute errors are 6.8 m and 4.9 m in the x and y directions, respectively.

Two sources (22 and 26) behave as clear outliers. We suspect that some of the propagation paths between these sources and the selected receivers contain artefacts, leading to relatively poor fits (misfit > 0.4) and consequently less accurate location estimates. We have added the following text to the manuscript to briefly comment on this:

When the source position is known, steps 2 and 3 of Algorithm 1 are not required and are therefore not presented here. Nevertheless, we verified that our algorithm is able to accurately recover the source locations. To this end, we selected the four corner stations together with one station located near the centre of the array. The mean absolute errors are 6.8 m and 4.9 m in the x and y directions, respectively, although two sources behave as clear outliers. We suspect that some of the propagation paths between these sources and the selected receivers are affected by artifacts, leading to relatively poor fits (misfit > 0.4) and consequently less accurate location estimates.

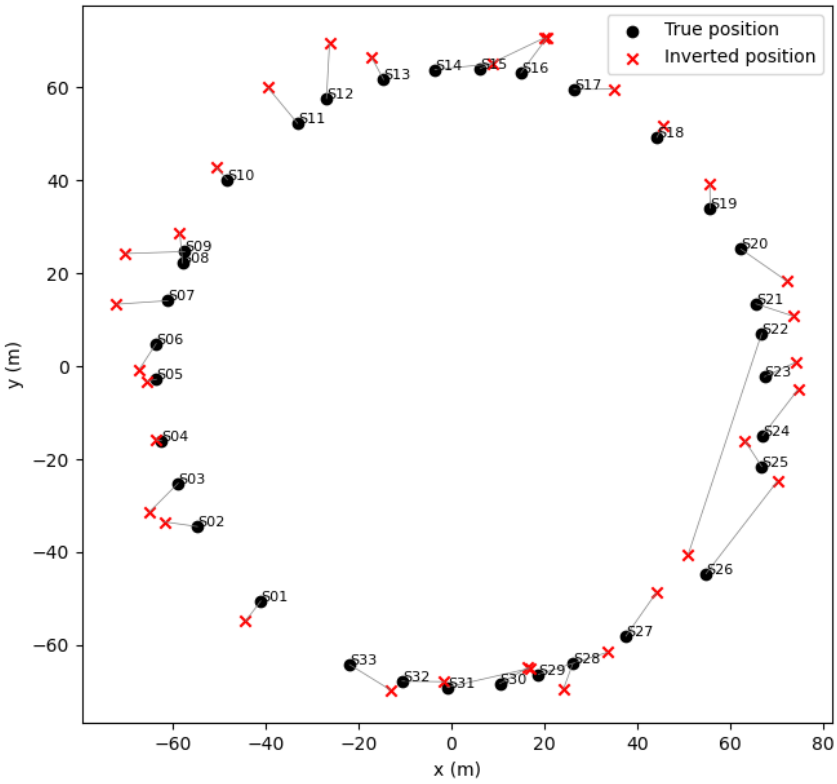


Figure 1: Comparison between the true source positions (black circles) and the positions recovered by the inversion (red crosses) for the artificial sources. Each pair is connected by a thin gray line to highlight the localization error for that source.

3 Potential sources of bias

3.1 The impact of ice variations along source-receiver paths

Given that the waveforms are based on constant ice thicknesses, what effect does the thickness gradient in the field have on the misfits?

We thank the reviewer for this question, which is also related to a comment of reviewer 2 on the effect of thickness variations along the paths.

The waveforms of the database are computed for a constant thickness, but the thickness retrieved on a path is an equivalent thickness: the thickness for which the accumulated phase is the same as in the ice of varying thickness along the path. The equivalent thickness equals the path-averaged thickness up to a second-order term, always negative, which does not exceed 1.2 cm for the thickness ranges of our data. This holds as long as the thickness varies slowly along the path, in the sense that the relative change of thickness over one wavelength is small, and if reflections and mode conversions are negligible. This analysis was added to the manuscript, and is copied below. We have also added a numerical verification and its limits in a new Appendix B, copied at the end of this answer to the reviewer.

Allowing a different thickness on each source–receiver path refines the level of detail with respect to Moreau et al. (2023), who assumed a single thickness for all paths of an event. However, each path thickness is still obtained by fitting a homogeneous-slab model to a waveform that has propagated through ice of varying thickness. The retrieved value is therefore an equivalent, or apparent, thickness. This is valid under the assumptions that the thickness varies slowly along the path. The phase of the flexural wave is then the integral of the local wavenumber, provided that the local wavenumber changes little over one wavelength λ and that reflections and mode conversions are negligible:

$$\frac{\lambda}{k}\left|\frac{\mathrm{d}k}{\mathrm{d}\ell}\right| \ll 1, \tag{7}$$

where ℓ is the curvilinear coordinate along the path. For the frequencies in this study, the water is deep enough for the gravity term of Eq. (2) to be negligible, so that:

$$k(h,\omega) = \left[12(1-\nu^2)\rho_w\omega^2/E\right]^{1/5} h^{-3/5} \tag{8}$$

Since the prefactor does not depend on the thickness, $\mathrm{d}k/k = -(3/5)\,\mathrm{d}h/h$, and Eq. (7) is equivalent to a condition on the relative thickness gradient:

$$\frac{\lambda}{h}\left|\frac{\mathrm{d}h}{\mathrm{d}\ell}\right| \ll 1. \tag{9}$$

For our data, with wavelengths of 8 to 18 m and thickness changes of 0.35 m or less over 200 to 600 m, this thickness-gradient parameter is about 0.05 or less.

In Appendix B, we demonstrate that, under this condition, the equivalent thickness is:

$$h_{\mathrm{eq}} \simeq \bar{h} + \frac{\Delta h^2}{24}\left.\frac{\partial^2 k/\partial h^2}{\partial k/\partial h}\right|_{\bar{h}}, \tag{10}$$

where $\bar{h}$ is the average thickness along the path. The numerical verification and the limits of this approximation are discussed in Appendix B, and our synthetic waveform tests with linear profiles confirm that the thickness fitted with a homogeneous slab agrees with the equivalent thickness within a fraction of a millimeter.

Because the wavenumber is a convex function of the thickness, the equivalent thickness is always smaller than the path-averaged thickness. To second order, the difference is $4\sigma_h^2/(5\bar{h})$, where σ_h^2 is the variance of the thickness along the path. For the thickness ranges of our datasets (0.50 to 0.85 m over 200 to 600 m), this term does not exceed 1.2 cm (less than 2%).

Under these assumptions, the waveform that has propagated through the ice of varying thickness is close to, but not identical to, the waveform of the equivalent thickness, because the equivalent thickness depends on frequency. In our synthetic tests, this dependence is very weak (the correction varies by less than 0.1 mm over the 5–40 Hz band), so that the constant-thickness waveform that best fits the data reproduces it closely and the misfit remains low.

In line 317 it is stated that 44% of the data at the controlled-source site is filtered away due to a too high misfit with waveforms in the generated database. According to line 311, one of the most common sources for these misfits are large cracks in the ice. How about ridges or deformed ice in general? The research by Xie & Farmers (1994) is mentioned in the introduction, but the influence of deformed ice is not discussed.

When the conditions above are not satisfied, the waveform is no longer well described by a constant thickness, and the misfit increases. This is the case for large cracks, but also for ridges or for strongly deformed ice, where abrupt changes of thickness or boundaries generate secondary reflections and mode conversions that distort the waveform and lead to large misfits. These paths are rejected by the misfit criterion, so that the criterion acts as a filter for the paths whose thickness cannot be interpreted as an equivalent thickness. A consequence is that the retained paths are, on average, those along which the thickness varies more smoothly, and the abrupt local variations are not constrained by these paths. The rejected paths (Figure 2) are rather randomly distributed, and not concentrated on the paths crossing the junction between the two blocks of ice of different thicknesses. This indicates that a thickness step of about 20 cm is not by itself the main cause of the rejections, and that the high misfits are rather related to local features along the paths. Finally, the thick ice of the experiment is a deformed ice with irregularities, and the thickness obtained agrees with the DAS inversion and with the drillings, which shows that a moderate deformation does not prevent the method from working.

44% is a very significant amount of data, so I suggest making a figure that shows which source-receiver paths were discarded. Are they randomly distributed or are they primarily paths that cross the transition between the two ice regions?

We agree with the reviewer, a figure showing the discarded paths would be informative. To address this, we are now showing the discarded paths next to those that are kept (see figure 2 below). As the reviewer points out, 44% of the data are rejected after removing outliers and measurements with large misfit. The rejected paths are shown in Figure 2 and exhibit a rather random spatial distribution.

We have added the following sentence to the manuscript, in the section describing the selection of the paths, to account for the two remarks by the reviewer:

The figure also shows the 232 rejected rays, which seem to be distributed randomly, including paths on both sides of the thickness discontinuity, as well as path that cross the discontinuity. The paths with a large misfit are mostly those along which the thickness is not slowly varying, for instance in the presence of large cracks, ridges or strongly deformed ice, which generate reflections and mode conversions that are not accounted for by a constant-thickness model. Rejecting them leaves the paths along which the thickness is well described by an equivalent thickness (see Appendix B).

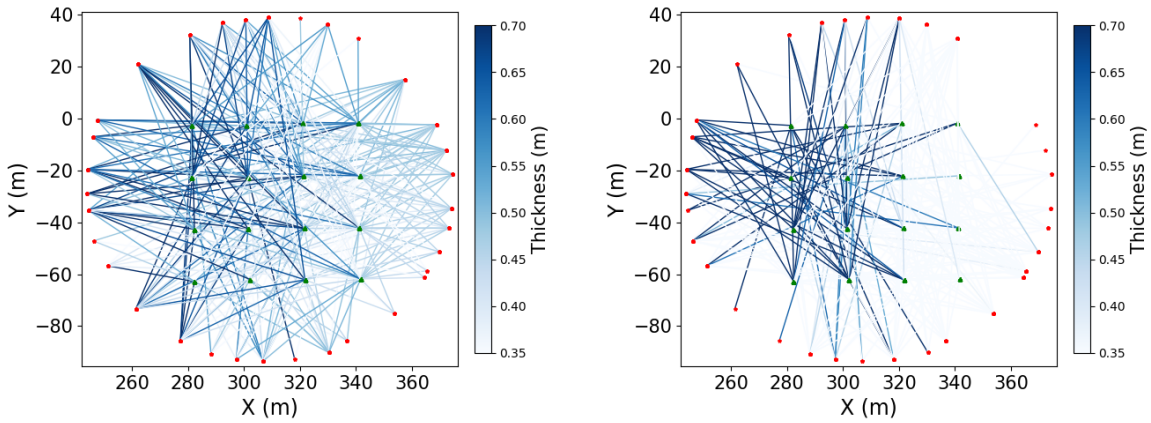


Figure 2: Spatial distribution of the selected (left, 296 paths) and rejected (right, 232 paths) source–receiver paths after applying the outlier and misfit criteria. The rejected paths account for 44% of the data.

As a follow-up question: In the current setup, the geophone grid is placed directly at the interface between the two ice regions, ensuring a handful of "pure paths" in each region. If the geophone grid instead were placed fully within one of the two regions, would it then have been possible to derive the thicknesses in the opposite region?

The thickness of a region without receivers can in principle be retrieved, provided that sources are located in it. The key requirement is not receiver coverage in each region, but path diversity: the fraction of each path lying in a given region must vary across paths. Pure paths within region A constrain h_A, while mixed paths crossing both regions constrain h_B through their fraction $f_{iB} = \ell_{iB}/L_i$, according to $h_{\mathrm{obs},i} \simeq (1 - f_{iB})h_A + f_{iB}h_B$. Pure paths alone would yield independent regional averages, without constraining the lateral transition; it is the mixed paths, with varying regional fractions, that provide the information needed for tomography across the interface.

The thickness of B is nevertheless less precisely resolved than that of A, because it is inferred only from mixed paths. An uncertainty δh_{obs} translates approximately into an uncertainty $\delta h_{\mathrm{obs}}/f_{iB}$ on h_B, in addition to the uncertainty on h_A: the amplification factor is 2 for $f_{iB} = 0.5$ and 5 for $f_{iB} = 0.2$. Mixed paths also provide lower resolution in B and are most affected by the difference between retrieved equivalent thickness and path-averaged thickness, although this difference remains small for the contrasts in our data (Appendix B). In our configuration, with the array on the interface and sources on both sides, both pure and mixed paths are available. If the array were entirely within one region, mixed paths would rely on sources in the other region, further reducing the precision on h_B.

Figure 3 shows the tomographies resulting from selecting only sources and receivers that are on separate sides of the thickness change. As explained above, each configuration constrains the tomography mainly in the areas most covered by the rays and, although the discontinuity can still be recovered, it is less apparent, due to the significantly reduced paths (only half the source-receiver pairs in each case).

While this is an interesting question, we believe this short analysis should not be included to the revised manuscript. We have added the following remark on this point in section 3.1 (*Inversion of controlled sources in Canada*), but a detailed analysis is beyond the scope of this work.

The configuration of the array, placed across the interface, allows source-receiver paths to cross the discontinuity, in addition to pure paths lying within each region. Had the array been located entirely within one region, the thickness of the other region could still, in principle, have been retrieved from mixed paths, provided that sources were located in it, but with a lower

precision, since it would then be constrained only by paths partly crossing that region.

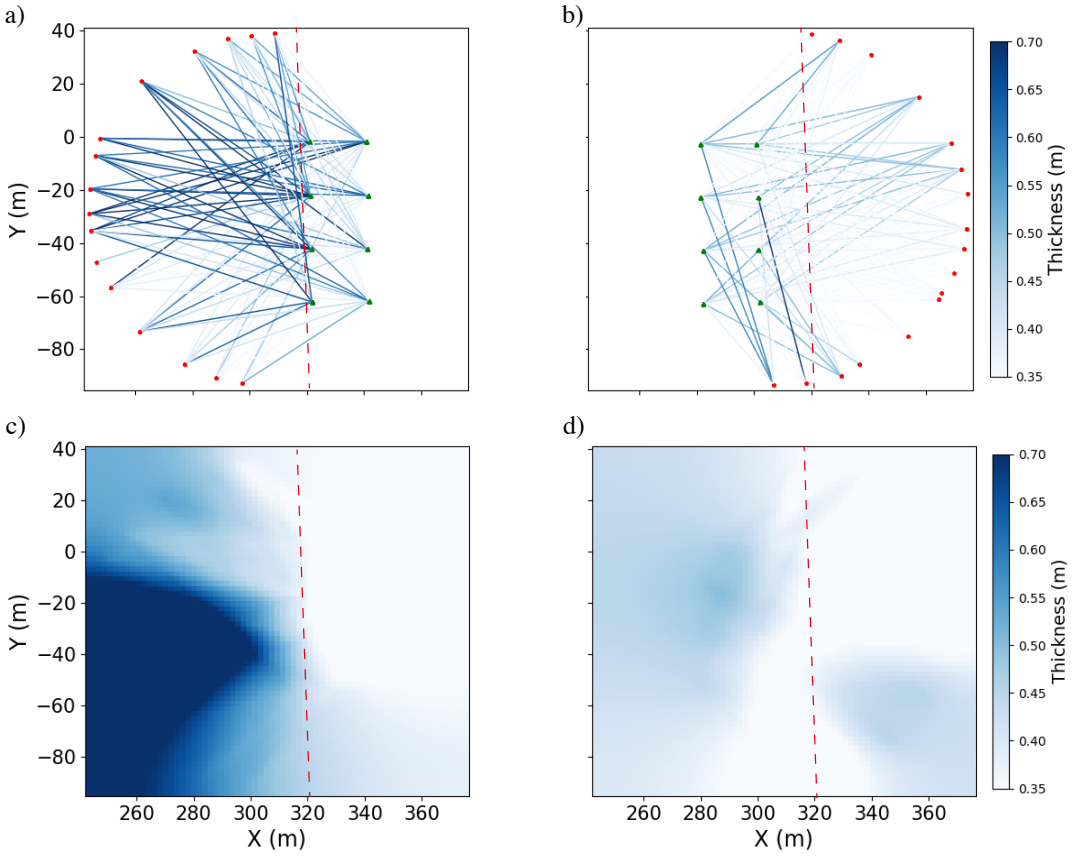


Figure 3: Seismic ray paths and corresponding tomographic reconstructions for two configurations: a) and c), using the eight remaining geophones after removing the first and second columns of the array and retaining only sources located to the left of the thickness change (90 paths); b) and d), using the eight remaining geophones after removing the third and fourth columns of the array and retaining only sources located to the right of the thickness change (111 paths). The red dots indicate the approximate position of the thickness change from the aerial photography in figure 1b

3.2 Sensitivity to temperature changes

During the duration of the time series in Vallunden, the air temperature rose from around -25° C to around -5° C according to line 125. Or below -30° C to close to 0° C according to line 375. I suggest that these descriptions are aligned.

We thank the reviewer for pointing out this inconsistency. We have revised the description in line 125 to be consistent with the temperature evolution described later in the manuscript. The air temperature dropped below −30 °C in early March and increased to values close to 0 °C toward the end of the recording period.

During the recording period, temperatures were below -30 °C in early March and progressively increased during the second half of March, reaching values close to 0 °C.

This was just a minor comment, and I wanted to bring focus on the significant temperature increase during the time series. In the discussion, line 420, the large uncertainty of Young's modulus is mentioned. It ranges from 1 GPa to 9GPa, but is assumed constant in the analysis. Young's modulus depends on the brine volume fraction of the ice which increases with rising temperatures. Thereby, the Young's modulus would decrease over time as the ice gets more compliant, leading to a negative thickness bias. I do not know if the magnitude of this bias is

significant, but I would have liked to read about it in the discussion given that the results are in general underestimated.

The reviewer is right, Young's modulus is, in general, impacted by changes in temperature. However, it should be mentioned that the ice was "insulated" by a layer of compacted snow with thickness about 30 cm. Moreover, Serripierri et al. (2022) showed that its effective value remained within $E = 3.7 \pm 0.4$ GPa over a 25-day period in Svalbard. This value is not a direct point measurement, but an effective elastic property of the ice layer sampled by the seismic wavefield within the dense array. It therefore represents an average property of the ice volume along the propagation path, which is the relevant scale controlling wave propagation.

The effect of possible temperature-induced variations in Young's modulus during the observation period is expected to be minor compared to the effect of ice thickness. As shown in Equation (3), the flexural rigidity,

$$D = \frac{Eh^3}{12(1-\nu^2)}, \tag{3}$$

depends linearly on E but scales with the cube of the ice thickness h. Therefore, variations in ice thickness have a much stronger influence on the dispersion characteristics of the QS mode than comparable variations in Young's modulus. For example, at a propagation distance of 250 m, thickness variations of only 2 cm (e.g., 48, 50, and 52 cm) produce waveform differences larger than those caused by variations in E from 3.3 to 4.1 GPa (Figure 4). Consequently, even if Young's modulus decreases slightly due to increasing temperature, the resulting bias on the estimated ice thickness remains negligible compared to the dominant sensitivity of the wavefield to ice thickness.

Considering that the influence is so small, and given that Young's modulus remained within $E = 3.7 \pm 0.4$ GPa over a 25-day period, we will just add one sentence to the manuscript to explain why we chose a constant value:

In this study, we use a constant Young's modulus of $E = 3.8$ GPa, based on the fact that Serripierri et al. (2022) reported values of $E = 3.7 \pm 0.4$ GPa over the 25 days of the experiment.

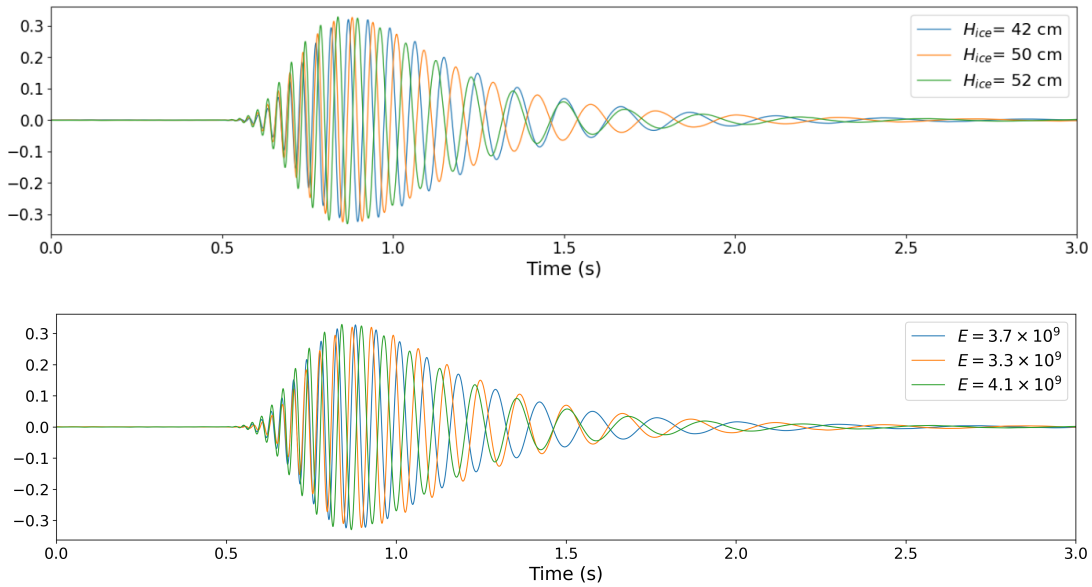


Figure 4: Comparison of waveform sensitivity to variations in ice thickness and Young's modulus. **Top:** Waveforms calculated for different ice thicknesses (48, 50, and 52 cm) while keeping Young's modulus constant ($E = 3.7$ GPa). **Bottom:** Waveforms calculated for different Young's modulus values (3.3, 3.7, and 4.1 GPa) while keeping ice thickness constant ($h = 50$ cm). Thickness variations produce significantly larger waveform differences than Young's modulus variations, highlighting the dominant sensitivity of the wavefield to ice thickness.

Nevertheless, our future work will investigate spatial and temporal variations of Young's modulus directly by extending the inversion framework to include E as a spatially varying parameter. Similar to the ice-thickness maps, this would require generating a SEM database for a range of Young's modulus values and performing an inversion to retrieve spatial variations in both ice thickness and elastic properties. This is part of the perspectives of the manuscript.

4 Optimal geophone setup for up-scaling

As one of the goals is to present a scalable solution for ice monitoring, as mentioned on line 11, I suggest discussing the potential up-scaling. I am especially interested in your thoughts on the optimal geophone setup. If you could re-do the experiments, would you change anything? The two field experiments have very different geophone grids, of which the first one is already reviewed in the part about potential biases. Looking at the generated time series maps, I cannot help but wonder why all the sensors were placed in the middle with such a high density (about 250 geophones in total with about 1 geophone pr. 10 m^2). Would it not improve the triangulation, result in a more constrained waveform matching, and lead to a higher spatial resolution (instead of radial rays) if the geophones were more spread out? At line 404 it is mentioned that "denser ray distributions, as well as broader and more uniform spatial coverage, result in more accurate thickness estimates".

We totally agree with the reviewer on that point. The dense Svalbard array was designed as a proof-of-concept experiment, to show that passive seismology can provide information on sea ice comparable to active experiments. At the time, we anticipated that heterogeneities, cracks, attenuation and porosity would prevent the waveforms from propagating more than a few tens of metres from their source, as is the case in the jumbled ice of the Canada experiment. Hence we configured the array for monitoring the ice at a smaller scale with conventional methods such as:

- noise interferometry to recover the Green's function between any sensor pair (Serripierri et al., 2022)
- tomography from the inter-sensor paths using the recovered Green's functions
- beamforming to characterize the azimuthal distribution of the wavefield and the source mechanisms (Moreau et al., 2020a)
- etc

Surprisingly, the data showed thousands of icequakes from distances of a few hundred meters, which opened new possibilities in terms of observation scale and source localization for tomography. But the geometry of the array was not optimal for this purpose. Nevertheless, we selected five stations from the full network, with the largest aperture possible and the best geometrical coverage (Figure 9 of the manuscript). The remaining stations provided additional thickness values for the tomography. As the reviewer suggests, some paths are close to parallel, because the stations are close to each other, so they mainly reduce the noise and improve the azimuthal coverage only marginally. If we had to redo the experiment, we would therefore deploy small antennae of 3–5 geophones covering a larger area of the fjord, rather than a dense array covering a small area, as suggested by the reviewer in the next question.

Just a suggestion after having read the manuscript: Would it make sense to have many clusters of geophones with at least 3 geophones in each cluster, such that each cluster can do an effective triangulation? Besides increasing the spatial coverage, it could reduce the mismatches from changing ice conditions because the ice could be measured from multiple sides with different clusters. And the lower density would make the up-scaling more feasible.

We agree that such clustered deployments are a promising strategy for large-scale passive monitoring. To illustrate the influence of the station geometry on the tomography, we performed a synthetic checkerboard test (Figures 5 and 6). Figure 5 shows the checkerboard model used to generate the thickness observations. In Figure 6(a), the stations are those of the original configuration used in the Svalbard experiment, and in Figure 6(b), they are relocated to cover the study area more broadly and uniformly. The corresponding tomographic results are shown in Figures 6(c) and 6(d). The broader geometry leads to a substantially better recovery of the checkerboard pattern, which shows that the station placement has a strong influence on the ray coverage and on the quality of the inversion.

The optimal design depends on the size of the monitored area (from a few hundred metres to several kilometres), on the propagation distance of the icequakes, on their expected distribution and on the desired resolution. For large areas, several small clusters would be an efficient alternative to a dense array. Determining the minimum number of stations and their optimal distribution for a given area requires a dedicated study.

To cover all these points, we have completely re-written the discussion section to include these comments to the manuscript.

A new Section 4.2, "Array geometry and up-scaling", has been added to the manuscript to address both comments, and thereafter. It discusses the influence of station geometry on ray coverage and tomographic resolution, the limitations of the original Svalbard array, and the potential benefits of more spatially distributed and clustered deployments for large-scale ice monitoring. It also presents synthetic checkerboard tests comparing the original configuration with a more spatially distributed array.

The dense Svalbard array was designed as a proof of concept to show that passive seismology can provide information on sea ice comparable to that obtained from active experiments. At the time, we anticipated that heterogeneities, cracks, attenuation, and porosity would prevent waveforms from propagating more than a few tens of metres from their sources, as is the case in the jumbled ice of the Canada experiment. The array was therefore designed for small-scale monitoring using conventional array methods: noise interferometry to recover the Green's function between sensor pairs, tomography based on inter-sensor paths, and beamforming to characterize the azimuthal distribution of the wavefield and the source mechanisms (Moreau et al., 2020a; Serripierri et al., 2022). These methods require a high density of sensors. Surprisingly, the data contained thousands of icequakes recorded at distances of a few hundred metres, opening the possibility of source localization and tomography at a larger scale. The array geometry was, however, not optimal for this purpose.

For event localization and path-thickness estimation, such a high station density is not required: five stations are sufficient for triangulation (Moreau et al., 2020b, 2023), and we used five stations selected for their large aperture and geometrical coverage. The other stations provide additional thickness estimates along nearly parallel paths, since they are close to each other. These additional measurements mainly help reduce the noise on the estimated thickness, while improving azimuthal coverage only marginally. Together with the sources, which are located mostly along the shoreline, a compact array produces rays that converge towards the array and images that are elongated along the ray directions.

The interpretation of small-scale thickness variations near the shoreline requires particular caution. Although many icequake sources are located along the shoreline, the resulting ray paths do not necessarily provide uniform spatial coverage or a broad range of azimuths near the sources. Moreover, rays originating from nearby sources may share common path segments, so that errors associated with these sources may be mapped into the same region rather than averaging out. Consequently, thickness estimates near the shoreline are less well constrained than in the central part of the array, where rays cross at different azimuths. Source-location errors may contribute to small-scale artefacts, although their estimated magnitude is insufficient to explain the largest observed thickness contrasts.

The ability to constrain a region depends not only on the number of paths but also on how they traverse the regions to be distinguished. Paths that do not cross a thickness contrast constrain the thickness along their trajectories but provide little information on the contrast between regions. The contrast between two regions, and the thickness of a region without receivers, can be constrained by paths that cross both regions. A region without any receiver can therefore be constrained if sources are located within it and if the fraction α of each path lying in this region varies between paths. In this case, an uncertainty δh_{obs} on the observed path thickness translates approximately into an uncertainty of $\delta h_{\mathrm{obs}}/\alpha$ on the thickness of the region, which increases as the fraction decreases.

The spatial resolution also depends on the wavelength of the flexural waves. For the ice properties listed in the table of mechanical parameters for Svalbard, the wavelength varies from approximately 20 m at 2 Hz to 5 m at 50 Hz. The icequake waveforms considered here are typically dominated by frequencies between 5 and 15 Hz, corresponding to wavelengths of approximately 8–18 m. These wavelengths provide a relevant physical scale for discussing spatial sensitivity, but the resolution of a tomographic image cannot be inferred from wavelength alone.

In finite-frequency travel-time tomography, a measurement is sensitive to a region around the geometrical ray rather than exclusively to the ray itself. An indicative transverse scale is provided by the first Fresnel zone, whose diameter at the midpoint of a source–receiver path of length L is approximately $D_F \simeq \sqrt{\lambda L}$. For wavelengths of 10–15 m and path lengths of 200–600 m, this gives diameters of approximately 45–95 m. This estimate illustrates the potential importance of finite-frequency effects, but it should not be interpreted as a strict lower bound on the tomographic resolution. The effective resolution also depends on the distribution and azimuthal diversity of the paths, measurement uncertainties, and the regularization and parameterization of the inversion.

Our inversion uses straight-ray sensitivity weights and does not explicitly account for finite-frequency effects. Consequently, narrow thickness anomalies located close to, but not intersected by, a geometrical ray may have a weaker influence on the measured waveform than predicted by the straight-ray approximation. Conversely, a set of paths with different azimuths and lengths can provide complementary constraints on the spatial distribution of thickness. The length scale that can actually be recovered must therefore be assessed for the acquisition geometry and inversion procedure considered here, rather than inferred from wavelength or ray density alone.

To illustrate the influence of station geometry on the recovery of spatial variations, we performed synthetic checkerboard tests (Figures 5 and 6). Figure 5 shows the checkerboard model used to generate the synthetic thickness observations. In Figure 6a, the stations are those of the original configuration used in the Svalbard experiment, whereas in Figure 6b they are relocated to provide broader and more uniform coverage of the study area. The corresponding tomographic results are shown in Figures 6c and d. The broader geometry leads to a substantially better recovery of the checkerboard pattern, demonstrating the strong influence of station placement on ray coverage and inversion quality. These tests provide an empirical assessment of the spatial scales recoverable with the tested geometries and inversion settings.

The optimal design depends on the size of the monitored area, from a few hundred metres to several kilometres, on the propagation distance and source distribution, and on the desired spatial resolution, but also on the ability of an icequake to propagate over long distances. Finally, long paths cross more thickness variations and cracks, making the assumption of slowly varying thickness more difficult to satisfy. Shorter paths are therefore more likely to meet this assumption, but require more stations or clusters to cover a given area. Determining the minimum number of stations and their optimal distribution for a given area and target resolution requires a dedicated study.

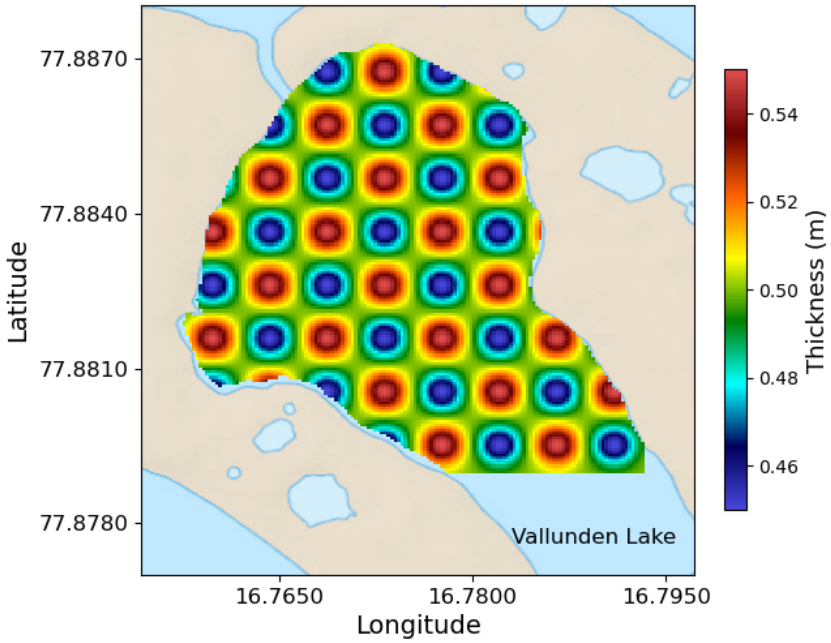


Figure 5: Synthetic checkerboard model used to generate the ice thickness observations for evaluating the influence of station geometry on the tomographic inversion.

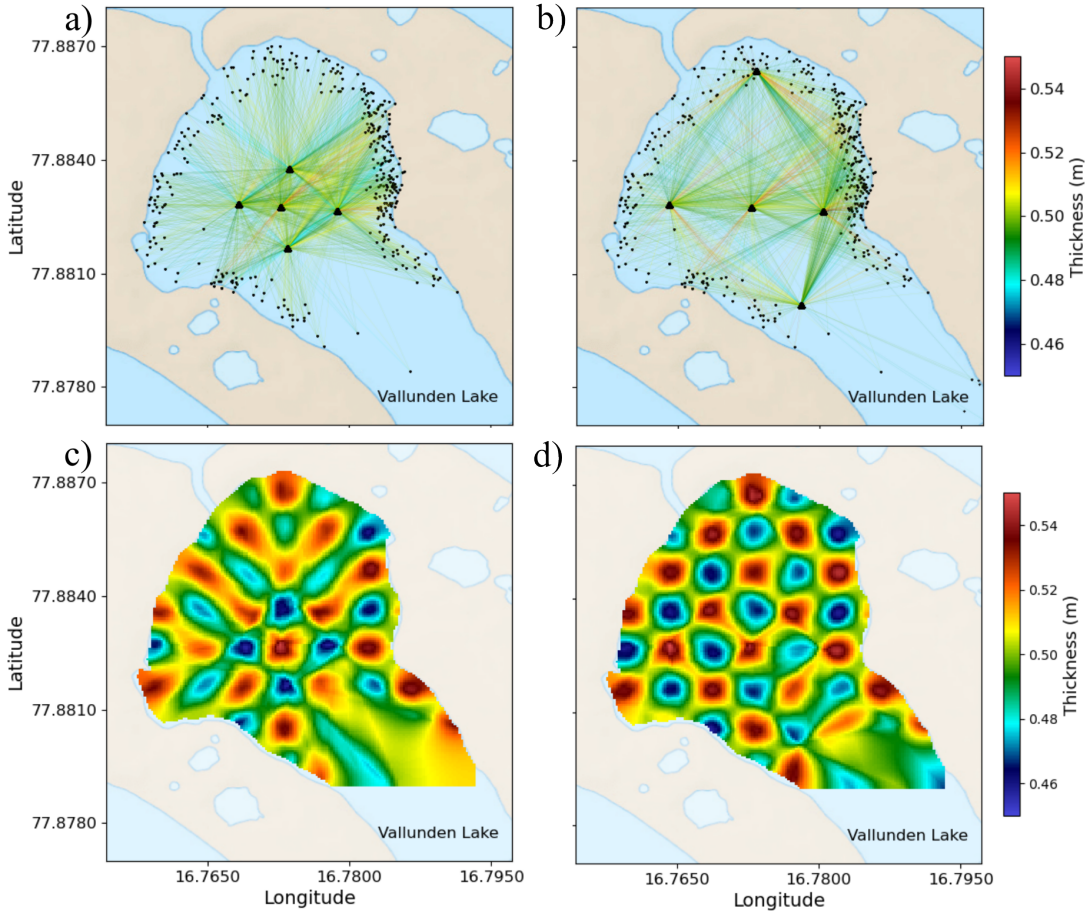


Figure 6: Influence of station geometry on tomographic reconstruction. (a) Original station configuration used for the first-step inversion to estimate ice thickness and source locations. (b) Optimized station configuration providing broader and more uniform ray coverage. (c) Tomographic inversion result using the original configuration. (d) Tomographic inversion result using the optimized configuration, showing an improved recovery of the checkerboard anomalies.

5 List of minor points

Title: "Temporal" should be capitalized for consistency.

Corrected accordingly, as suggested by the reviewer.

Line 276: . . . zero of the misfit function . . .

Corrected as: obtained by setting the gradient of the objective function to zero

Figure 8: There is an extra "a)" in the beginning of the caption.

Corrected accordingly, as suggested by the reviewer.

Figure 8: If (0212) and (0206) are dates, 12 Feb and 6 Feb is clearer without context.

Corrected accordingly, as suggested by the reviewer.

Figure 9: "b),c)" error in the caption.

Corrected as: Comparison between the method of Moreau et al. (2023) and the method described in Section 2.3.2: a) comparison of the relocated icequake positions, and (b,c) comparison of the inverted waveforms obtained using the method of Moreau et al. (2023) (red) and the method described in Section 2.3.2 (green).

Line 360: Besides the faster cooling at shallower water depths, could the thicker ice also be due to dynamical thickening from tides?

Yes, tidal dynamical thickening from frazil/crystal transport could contribute, as shown by Marchenko et al. (2021), but this effect is confined to the area near the main channel and stops

by mid-March. In our study area, away from the channel, the dominant mechanism remains thermodynamic growth due to shallower water depths, as stated in the original text.

We have added the following sentence to the manuscript:

Tidal currents may also contribute to local ice thickening near the northern channel by transporting ice crystals and cold water beneath the ice Marchenko et al. (2021).

Figure 14: A legend would suit this figure.

Corrected accordingly, as suggested by the reviewer.

Line 413: Random question mark mid-sentence.

Thank you for pointing this out. The question mark resulted from a missing reference, which has now been corrected.

Line 449: The end of the conclusion focuses on future developments regarding extending the framework to include heterogeneity, anisotropy, and snow cover. This needs to be mentioned in the discussion as well.

Thank you for this suggestion. We have added a new paragraph at the end of the Discussion section addressing the potential extension of the framework to account for ice heterogeneity, anisotropy, and snow cover.

A natural extension of this work is to include more realistic ice physics in the forward modeling and inversion framework. The current study assumes a homogeneous, isotropic, and snow-free ice layer, which is a useful first approximation but does not fully represent natural sea ice. In reality, ice can be heterogeneous and anisotropic due to temperature variations, brine, air bubbles, cracks, and crystal orientation. Snow cover can also affect the dispersion of flexural waves.

Extending the spectral-element database and inversion framework to account for these effects, for example through depth-dependent or anisotropic elastic properties and the inclusion of a snow layer, would improve thickness estimates in more complex environments and represents a promising direction for future research.

5.1 2.3.1 Construction of a SEM database

I understand that for each discrete source-receiver distance, the database has a range of derived waveforms corresponding to a range of discrete ice thicknesses. Thereby the number of waveforms would equal the product of distance steps and thickness steps.

The formulation explaining this, line 221, is confusing. The variables x and y are defined as the respective intervals, i.e., step sizes, together with xx and yy as the maximum distance and thickness, respectively. This results in z waveforms. Besides being confusing, these variables are not used later on, and both x and y are redefined in section 2.3.3 for the tomography computation. Are they needed? I think it would be more informative to know the actual number of waveforms in the database and the actual used ranges - together with a justification of chosen limits.

Thank you for pointing this out. We have replaced it with a new paragraph to clarify this point.

To remedy this issue, we build "offline" databases of seismic waveforms parameterized by the source–receiver distance and the ice thickness. For the active-source dataset in Canada, the database includes source–receiver distances ranging from 1 to 200 m, sampled every 1 m, and ice thicknesses ranging from 10 to 100 cm, sampled every 1 cm. This results in 18,200 waveforms. For the natural-source dataset in Svalbard, the database includes source–receiver distances ranging from 1 to 620 m, sampled every 1 m, and ice thicknesses ranging from 20 to 100 cm, sampled every 1 cm, resulting in 50,220 waveforms. These ranges cover the distances and ice-thickness values considered in the two datasets. The simulations are performed on the local computing facilities of the Univ. Grenoble Alpes. For the active-source simulations, the ice mechanical parameters are taken from Kuchly et al. (2026), while the parameters used for the natural-source simulations are based on Serripierri et al. (2022). The source-time function used for each simulation is calibrated to cover the frequency range of the corresponding seismic data.

6 Conclusion

The manuscript covers a novel and fascinating way of monitoring the sea ice thickness of a local area with high spatial resolution. Unfortunately, the analysis does not demonstrate that the approach is robust across different environments as stated in the conclusion - and it does not demonstrate the opposite either.

About 44% of the data in the controlled-source experiment is filtered away without a detailed description of given data, and there is no discussion on the influence of deformed ice or varying ice thicknesses on the waveform matchings.

I suggest being more clear about potential limitations of the method and a discussion on how to mitigate them. That would include thoughts on how to place the geophones most optimally for future experiments, and if there are hypothetical cases where this method cannot be applied.

Based on these two points specifically, but also with a smaller emphasis on the other points mentioned in this review, a major revision is suggested.

Once again, we would like to thank the reviewer for the useful comments. We have addressed all of them in detail: the rejected data and the influence of deformed ice and thickness variations are discussed in Section 3, the geophone placement and the limitations of the method in Section 4, and the validation of the results in Section 2. We hope these answers make all the points raised by the reviewer clearer.

Appendix B: Equivalent thickness and path-averaged thickness

This appendix details the relation between the thickness retrieved by fitting a constant-thickness model to a waveform that has propagated through ice of varying thickness (the equivalent thickness $h_{\mathrm{eq}} = h_{\mathrm{obs},i}$) and the path-averaged thickness $\bar{h} = \langle h \rangle$ used in Eq. (11).

B1: Definition of the equivalent thickness

For a given angular frequency ω, the wavenumber $k(h,\omega)$ of the flexural–gravity wave in ice of thickness h is the root of the dispersion relation, Eq. (2). When the thickness varies slowly along a path of length L, $h = h(x)$ with $0 \le x \le L$, the phase accumulated over the path is the integral of the local wavenumber as in the path-average treatment of surface waves (Woodhouse and Dziewonski, 1984; Kennett and Yoshizawa, 2002), and for guided modes in waveguides of linearly varying thickness (Moreau et al., 2014):

$$\varphi(\omega) = \int_0^L k\big(h(x),\omega\big)\,\mathrm{d}x. \tag{23}$$

A constant-thickness model with thickness h_c gives $\varphi_c(\omega) = k(h_c,\omega)\,L$. Both have the same dispersion, and hence the same waveform shape, if

$$k\big(h_{\mathrm{eq}},\omega\big) = \frac{1}{L}\int_0^L k\big(h(x),\omega\big)\,\mathrm{d}x = \langle k \rangle, \tag{24}$$

where $\langle\cdot\rangle$ is the average along the path. This is Eq. (12) with $h_{\mathrm{eq}} = h_{\mathrm{obs},i}$. The equivalent thickness is therefore the thickness whose wavenumber equals the path average of the wavenumber, and not the thickness whose value equals the path average of the thickness. Because k is a nonlinear function of h, these two averages differ in general. The same distinction arises in near-surface surface-wave analysis (Boiero and Socco, 2011).

B2: Exact result for a linear profile and second-order expansion

In the flexural regime, Eq. (2) reduces to $k \propto h^{-3/5}$, and Eq. (24) leads to the power mean of Eq. (13). For a thickness varying linearly from h_1 to h_2 along the path, the integral can be

computed exactly:

$$h_{\mathrm{eq}} = \left[\frac{5}{2} \, \frac{h_2^{2/5} - h_1^{2/5}}{h_2 - h_1} \right]^{-5/3} . \tag{25}$$

We write $h_{1,2} = \bar{h}(1 \mp \varepsilon)$, with $\varepsilon = \Delta h/(2\bar{h})$ and $\Delta h = |h_2 - h_1|$. Exchanging h_1 and h_2 leaves the result unchanged, so only even powers of ε appear:

$$h_{\mathrm{eq}} = \bar{h} \left[1 - \frac{4}{15} \, \varepsilon^2 - 0.068 \, \varepsilon^4 + \dots \right] \simeq \bar{h} - \frac{\Delta h^2}{15 \, \bar{h}} . \tag{26}$$

The total relative change ε is not small compared with one ($\varepsilon \leq 0.26$ for the thickness ranges of our data), so the truncation is not justified by a small-variation argument but was checked numerically against the exact Eq. (25): for $\varepsilon \leq 0.26$ the two differ by about 0.2 mm at most (the term in ε^4 is less than 2% of the one retained), and the relative bias does not exceed 1.8%. Even for a stronger contrast, 0.80 to 0.35 m ($\varepsilon = 0.39$), the correction is 23.5 mm with Eq. (26) against 24.5 mm with Eq. (25).

The same result follows from a perturbation expansion of k about $\bar{h}$ for the linear profile, whose local deviation $h(x) - \bar{h}$ takes all values between $-\Delta h/2$ and $\Delta h/2$ with equal weight, so that its path average is zero and its variance is $\sigma_h^2 = \Delta h^2/12$:

$$k\big(h(x), \omega\big) \simeq k(\bar{h}) + \left. \frac{\partial k}{\partial h} \right|_{\bar{h}} \big[h(x) - \bar{h} \big] + \frac{1}{2} \left. \frac{\partial^2 k}{\partial h^2} \right|_{\bar{h}} \big[h(x) - \bar{h} \big]^2 . \tag{27}$$

Averaging along the path, the first-order term vanishes and $\langle k \rangle \simeq k(\bar{h}) + \frac{\Delta h^2}{24} \, \partial^2 k/\partial h^2$. Expanding the left-hand side of Eq. (24) to first order and equating both expressions gives

$$h_{\mathrm{eq}} \simeq \bar{h} + \frac{\Delta h^2}{24} \left. \frac{\partial^2 k/\partial h^2}{\partial k/\partial h} \right|_{\bar{h}} , \tag{28}$$

where the derivatives follow from implicit differentiation of Eq. (2). For $k \propto h^{-3/5}$ the ratio of derivatives is $-8/(5\bar{h})$, which gives back Eq. (26). The correction is even in Δh, so it is identical for a thickness increasing or decreasing along the path. Moreover, k decreases with h and is convex, so that $k(h) \geq k(\bar{h}) + \partial k/\partial h|_{\bar{h}} \, (h - \bar{h})$. Averaging along the path gives $\langle k \rangle \geq k(\bar{h})$ and hence $h_{\mathrm{eq}} \leq \bar{h}$ for any thickness profile, not only for a linear one.

B3: Effect of the source spectrum

The fit is performed on a band-limited pulse and not at a single frequency. Equation (24) holds at each frequency, so the equivalent thickness is in principle frequency dependent, and the fitted thickness is a weighted average of $h_{\mathrm{eq}}(\omega)$ over the source spectrum. This weighting has a negligible effect because the correction of Eq. (28) depends on frequency only through the local exponent of $k(h)$. The inertia of the ice makes this exponent vary slightly with frequency, from -0.58 to -0.57 between 5 and 40 Hz, because the ratio of the inertia of the ice to that of the water loading increases with the wavenumber. Evaluating Eq. (28) with the full dispersion relation, Eq. (2), from 5 to 40 Hz, the correction varies by less than 0.1 mm (for $\bar{h} = 0.675$ m and $\Delta h = 0.35$ m it is -12.0 mm over the whole band, against -12.1 mm for the pure power law).

B4: Numerical verification with synthetic waveforms

We generated waveforms for a linear thickness profile by integrating the local wavenumber obtained from Eq. (2) along x, and searched, with a constant-thickness model, for the thickness that maximizes the normalized cross-correlation. The source was a Gaussian-windowed pulse centered at $f_0 = 5$, 10 and 15 Hz, with propagation distances $L = 200$ to 600 m, and $H = 1200$ m,

Profile	$\bar{h}$ (m)	Δh (m)	$\bar{h} - h_{\mathrm{eq}}$ fitted (mm)	$\bar{h} - h_{\mathrm{eq}}$ Eq. (28) (mm)
0.725 → 0.625 m	0.675	0.10	1.0	1.0
0.750 → 0.600 m	0.675	0.15	2.2	2.2
0.775 → 0.575 m	0.675	0.20	3.9	3.9
0.800 → 0.550 m	0.675	0.25	6.2	6.1
0.825 → 0.525 m	0.675	0.30	8.9	8.8
0.850 → 0.500 m	0.675	0.35	12.2	12.0

Table B-1: Bias of the path-averaged thickness with respect to the fitted equivalent thickness, for a thickness decreasing along the path. For each contrast, 15 simulations were run (L = 200, 300, 400, 500, 600 m and f_0 = 5, 10, 15 Hz). The fitted bias is the mean over these 15 cases; it varies by less than 0.05 mm between cases. The second-order estimate of Eq. (28), evaluated with the full dispersion relation, does not depend on L or f_0, and differs from the fitted value by less than 0.25 mm in all cases.

E = 3.8 GPa, ν = 0.321, ρ_i = 910 and ρ_w = 1010 kg m^{-3}. The fitted thickness changed by less than 0.2 mm between increasing and decreasing profiles, and by less than 0.05 mm between distances and frequencies (Table B-1).

For the sharpest contrast of our data (0.50 to 0.85 m), the equivalent thickness is therefore smaller than the mean thickness by at most 1.2 cm (less than 2%). Identifying the retrieved thickness with the path-averaged thickness thus introduces a systematic underestimation of at most this size. Its sign is known, and it can be corrected with Eq. (28).

B5: Limits

The bias grows as Δh^2 and, at fixed Δh, as the mean thickness decreases (it depends on the relative contrast $\Delta h/\bar{h}$). For thinner ice and stronger contrasts, such as 0.30 to 0.80 m and 0.20 to 0.70 m over 200 m, we find a bias of about 3 and 4 cm (6% and 9%), and the second-order formula then deviates from the fitted value by 1.6 and 3 mm. These cases are outside the range of our data. The tests also assume a linear thickness profile, a slowly varying thickness (no mode conversion or reflection) and noise-free synthetic waveforms. For non-linear profiles, Eq. (13) or Eq. (24) can be used directly instead of Eq. (28); the sign of the bias remains the same by convexity of k.

Appendix C: Checkerboard Resolution Tests

This appendix presents synthetic checkerboard tests designed to evaluate the spatial resolution of the ice-thickness tomographic inversion for the controlled-source and natural-source datasets. Synthetic thickness models with alternating anomalies of different spatial scales are used to assess how well the inversion recovers the imposed patterns under the ray coverage of each experiment.

C1: Controlled-source data

Three checkerboard tests with different anomaly sizes are performed to assess the spatial resolution of the controlled-source tomographic inversion. The tests use the 296 selected paths out of 528 possible paths.

C2: Natural-source data

Checkerboard tests are performed using paths retained after quality control. Results are pre-

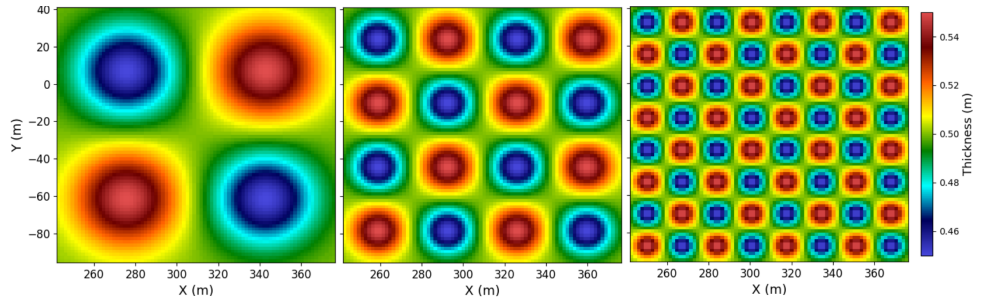


Figure C-1: Synthetic checkerboard models used for the controlled-source resolution tests.

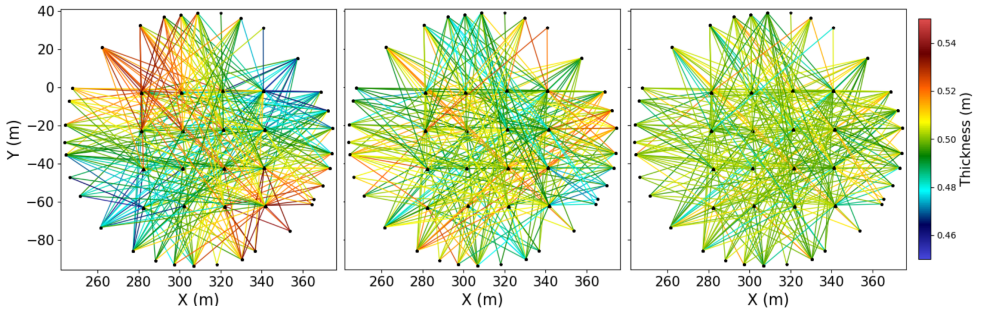


Figure C-2: Source–receiver paths for the 296 selected paths, colored according to their thickness values, as indicated by the colorbar.

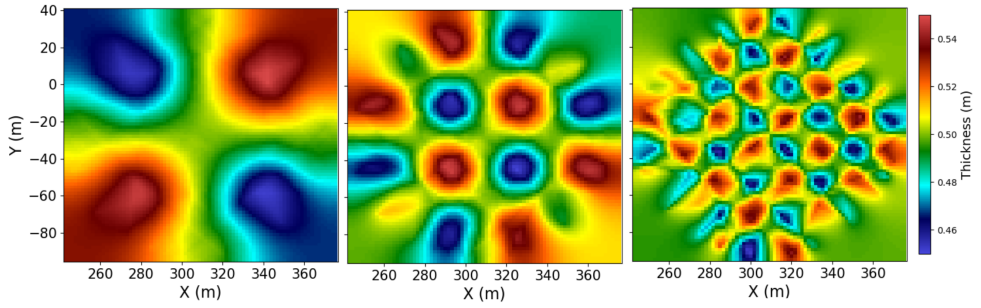


Figure C-3: Tomographic reconstructions of the three synthetic checkerboard models for the controlled-source dataset.

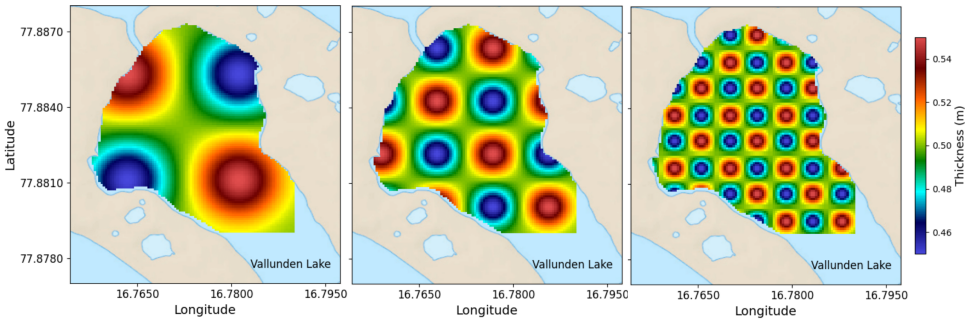


Figure C-4: Synthetic checkerboard models used for the natural-source resolution tests.

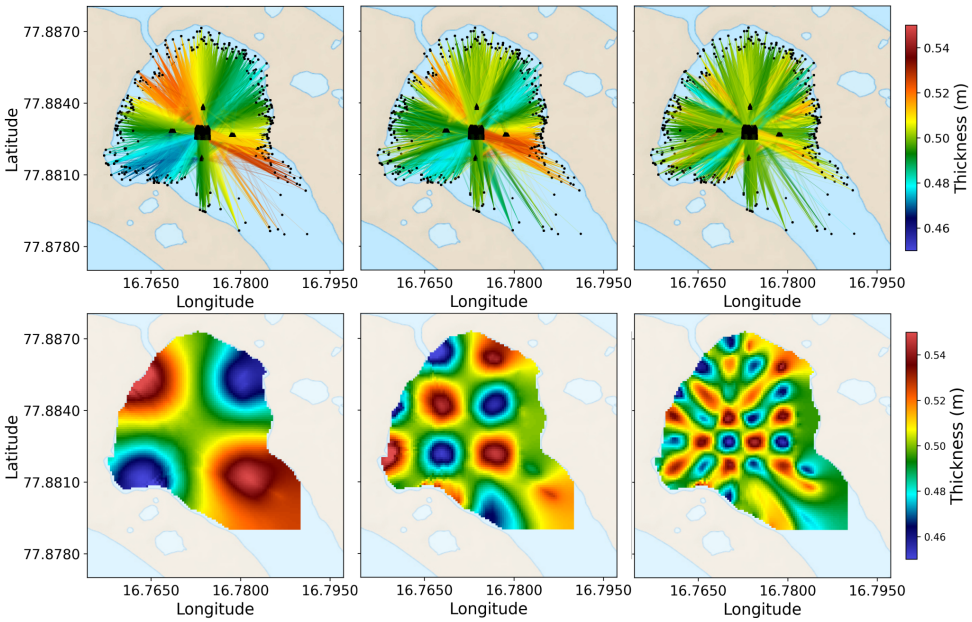


Figure C-5: Source–receiver paths for the selected paths, colored according to their thickness values (top), and the corresponding tomographic reconstructions for 7 March 2019 (bottom).

sented for 7 March 2019, one of the days with the best path coverage, and 18 March 2019, which has the fewest paths and the poorest coverage.

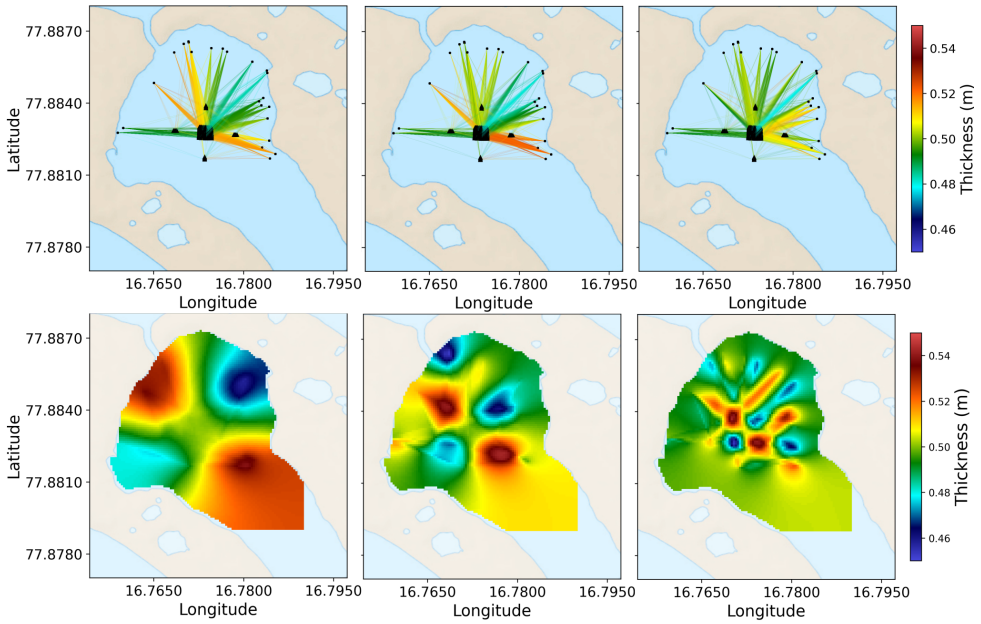


Figure C-6: Source–receiver paths for the selected paths, colored according to their thickness values (top), and the corresponding tomographic reconstructions for 18 March 2019 (bottom).

References

Boiero, D. and Socco, L. V.: The meaning of surface wave dispersion curves in weakly laterally varying structures, Near Surface Geophysics, 9, 561–570, 2011.

Kennett, B. and Yoshizawa, K.: A reappraisal of regional surface wave tomography, Geophysical Journal International, 150, 37–44, 2002.

Kuchly, S., Moreau, L., Zanchi, V., Mokus, N., Dansereau, V., Smith, M. M., Dumont, D., Perrard, S., and Eddi, A.: High-Resolution Measurement of Sea Ice Mechanical Characteristics Using Distributed Acoustic Sensing, Seismological Research Letters, (under review), 2026.

Marchenko, A., Morozov, E., Ivanov, A., Elizarova, T., and Frey, D.: Ice thickening caused by freezing of tidal jet, Russian Journal of Earth Sciences, 21, 1–8, https://doi.org/10.2205/2021ES000761, 2021.

Moreau, L., Minonzio, J.-G., Talmant, M., and Laugier, P.: Measuring the wavenumber of guided modes in waveguides with linearly varying thickness, The Journal of the Acoustical Society of America, 135, 2614–2624, https://doi.org/10.1121/1.4869691, 2014.

Moreau, L., Boué, P., Serripierri, A., Weiss, J., Hollis, D., Pondaven, I., Vial, B., Garambois, S., Larose, É., Helmstetter, A., Stehly, L., Hillers, G., and Gilbert, O.: Sea Ice Thickness and Elastic Properties From the Analysis of Multimodal Guided Wave Propagation Measured With a Passive Seismic Array, Journal of Geophysical Research: Oceans, 125, e2019JC015 709, https://doi.org/10.1029/2019JC015709, 2020a.

Moreau, L., Weiss, J., and Marsan, D.: Accurate Estimations of Sea-Ice Thickness and Elastic Properties From Seismic Noise Recorded With a Minimal Number of Geophones: From Thin Landfast Ice to Thick Pack Ice, Journal of Geophysical Research: Oceans, 125, e2020JC016 492, https://doi.org/10.1029/2020JC016492, 2020b.

Moreau, L., Seydoux, L., Weiss, J., and Campillo, M.: Analysis of microseismicity in sea ice with

deep learning and Bayesian inference: application to high-resolution thickness monitoring, The Cryosphere, 17, 1327–1341, https://doi.org/10.5194/tc-17-1327-2023, 2023.

Serripierri, A., Moreau, L., Boue, P., Weiss, J., and Roux, P.: Recovering and monitoring the thickness, density, and elastic properties of sea ice from seismic noise recorded in Svalbard, The Cryosphere, 16, 2527–2543, https://doi.org/10.5194/tc-16-2527-2022, 2022.

Woodhouse, J. and Dziewonski, A.: Mapping the upper mantle: Three dimensional modelling of earth structure by inversion of seismic waveforms, Journal of Geophysical Research, 89, 5953–5986, 1984.